Modeling of Magnetically Levitated Planar Actuators With Moving Magnets

J. W. Jansen, C. M. M. van Lierop, E. A. Lomonova, and A. J. A. Vandenput

Department of Electrical Engineering, Eindhoven University of Technology, Den Dolech 2, 5612 AZ Eindhoven, The Netherlands

This paper presents three types of magnetostatic models of ironless planar actuators with moving magnets. The models predict the force and torque exerted on the translator of the actuator, which can be positioned in six degrees-of-freedom with respect to the stator coils. The force and torque are calculated with the Lorentz force law. The analytical and numerical models can be used for the design of large planar actuators, for the fast comparison of actuator topologies, and in the decoupling and commutation algorithm. The models have been verified with experiments.

***Index Terms*—Electromagnetic analysis, linear synchronous motors, magnetic levitation, modeling, numerical analysis, permanent magnets, planar actuators.**

I. Introduction

In recent years, magnetically levitated ac synchronous planar actuators have been developed as an alternative to xy-drives constructed of stacked linear actuators in demanding applications such as semiconductor lithography systems. Although the translator of these ironless planar actuators can move over relatively large distances in the xy-plane only, it has to be controlled in six degrees-of-freedom (6-DOF) because of the active magnetic bearing. These actuators have either moving magnets and stationary coils [1], [2] or moving coils and stationary magnets [3]. The coils in the actuator are simultaneously used for propulsion in the xy-plane as well as for the 4-DOF active magnetic bearing. In [7], [11], and [12], planar actuators with mechanical bearings also are described.

In this research, a long-stroke moving-magnet planar actuator is investigated. Fig. 1 shows an overview of such an actuator [13]. The advantage of a moving-magnet actuator over a moving-coil actuator is that no cable to the translator of the actuator is necessary. Because only the coils below and near the periphery of the magnet array can produce force and torque, switching between different sets of coils is required during the movement of the translator. Although the actuator has certain similarities with synchronous machines, DQ0-decomposition cannot be used for the decoupling of the force and the torque. Therefore, new decoupling and commutation methods have been developed and every coil is excited with a single-phase power amplifier [4]. To design and simulate moving-magnet planar actuators, to investigate the influence of the new commutation algorithm, and to compare topologies, fast and accurate models are needed in which the full planar motor can be simulated.

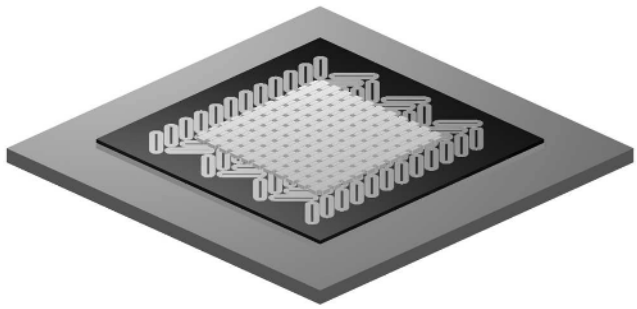

Fig. 1. Moving-magnet planar actuator.

In literature, several electromechanical models for planar motors can be found. In [5], a method is briefly described to model the force and torque in a moving-coil planar actuator. This approach uses magnetic surface charges to model the permanent magnets. However, [5] does not give details about the method and its implementation. Reference [6] presents a model of an ironless linear actuator. This two-dimensional model uses Fourier analysis for the calculation of the force in the actuator. In [7], Fourier analysis of a three-dimensional (3-D) infinitely large magnet array is used to calculate the magnetic flux density distribution and the propulsion force in a coreless planar actuator. In both [6] and [7], no expressions for the torque are derived.

This paper presents a complete magnetostatic analysis framework for moving-magnet planar actuators. Three methods which calculate both the force and torque in moving-magnet planar actuators, based upon the Lorentz force law, are presented in detail. Contrary to finite-element methods, these models are capable of simulating large planar actuators. The first method is based on magnetic surface charges. This numerical model allows to position the translator, which contains the permanent magnets, in 6-DOF with respect to the coil array. The second method uses Fourier series to model the magnetic flux density distribution of the magnet array. The method is

Digital Object Identifier 10.1109/TMAG.2006.886051

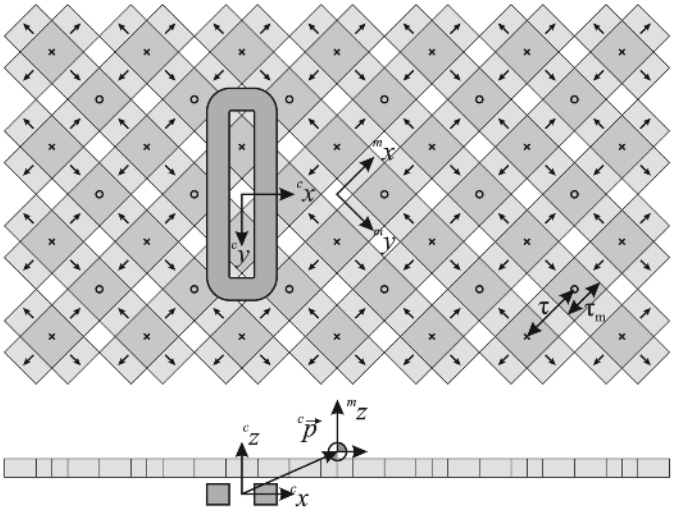

Fig. 2. Bottom and side view of the components of a moving-magnet planar actuator: a Halbach magnet array and a coil. Definition of the coordinate systems.

implemented for the most part analytically and, consequently, planar actuators can be evaluated in a very short time. The last method is a fully analytical method which can be evaluated in real-time. This model can be used in the decoupling algorithm of planar actuators. All models are validated with experiments on a 3-DOF magnetically levitated linear actuator.

II. Force and Torque Production

The moving-magnet planar actuators, which can be analyzed with the presented methods, are constructed of a permanent-magnet array with cuboidal magnets and coreless coils. Fig. 2 shows these elements of the planar actuator. The magnet array is a Halbach array to increase the magnetic flux density near the coil. The coil is placed at an angle of 45° with respect to the magnets [3]. As a result, the size of the coil is not limited to the pole pitch as in [2], and coils can be optimized to produce only force in the x- and z-directions or the y- and z-directions.

The force on the translator of the moving-magnet planar actuator is opposite to the force on the stator coil and can be calculated with the Lorentz force equation, as the coils are coreless. To calculate the torque on the translator, the force distribution in the coil has to be taken into account. The force on the translator can be modeled to act in the volume of the coil itself. Therefore, the force arm is defined from the mass center point of the translator to within the volume of the coil. Consequently, the force arm varies with the position of the translator. On the contrary, the force arm in a moving-coil planar actuator is independent of the position of the translator, as the coils are located on the moving part of the actuator itself.

The planar actuator has an active magnetic bearing, which can only be stabilized in 6-DOF with feedback control. At least six individually energized coils are necessary to control the translator. If the translator can be modeled as a rigid body, the total force and torque is the sum of the individual contributions of the coils. For that reason, the models are derived for one coil only. The synthesis and the optimization of topologies with multiple coils are outside the scope of this paper.

III. Coordinate System Definitions

Two coordinate systems are defined in the 3-D Euclidian space to model the actuator. These coordinate systems are shown in Fig. 2. The global coordinate system is defined at the stationary part of the actuator. In this coordinate system the coils are defined. For that reason it is denoted with the superscript ^{c}

$$ {}^c\vec{x} = [{}^cx \quad {}^cy \quad {}^cz]^{\mathsf{T}}. \tag{1} $$

A local coordinate system is defined in the mass center point of the translator. In this coordinate system the magnets are defined. For that reason, it is denoted with the superscript ^{m}

$$ {}^m\vec{x} = [{}^mx \quad {}^my \quad {}^mz]^{\mathsf{T}}. \tag{2} $$

The vector

$$ {}^c\vec{p} = [{}^cp_x \quad {}^cp_y \quad {}^cp_z]^{\mathsf{T}} \tag{3} $$

defines the position of the local coordinate system, i.e., the mass center point of the translator, expressed in the global coordinates.

Coordinates are transformed from one system to the other with an orientation transformation and afterwards a translation. The transformation matrix $^{\mathbf{c}}\mathbf{T_m}$ for a position from the local to the global coordinate system is equal to [8]

$$ {}^{\mathbf{c}}\mathbf{T_m} = \begin{pmatrix} {}^{\mathbf{c}}\mathbf{R_m} & {}^c\vec{p} \\ 0 & 1 \end{pmatrix}. \tag{4} $$

For convenience, the orientation transformation matrix is defined as

$$ {}^{\mathbf{c}}\mathbf{R_m} = \mathbf{Rot}({}^cy,{}^m\theta)\mathbf{Rot}({}^cx,{}^m\psi)\mathbf{Rot}({}^cz,{}^m\phi) \tag{5} $$

where

$$ \mathbf{Rot}({}^cy,{}^m\theta) = \begin{pmatrix} \cos({}^m\theta) & 0 & \sin({}^m\theta) \\ 0 & 1 & 0 \\ -\sin({}^m\theta) & 0 & \cos({}^m\theta) \end{pmatrix} \tag{6} $$

$$ \mathbf{Rot}({}^cx,{}^m\psi) = \begin{pmatrix} 1 & 0 & 0 \\ 0 & \cos({}^m\psi) & -\sin({}^m\psi) \\ 0 & \sin({}^m\psi) & \cos({}^m\psi) \end{pmatrix} \tag{7} $$

$$ \mathbf{Rot}({}^cz,{}^m\phi) = \begin{pmatrix} \cos({}^m\phi) & -\sin({}^m\phi) & 0 \\ \sin({}^m\phi) & \cos({}^m\phi) & 0 \\ 0 & 0 & 1 \end{pmatrix} \tag{8} $$

and where $^m\psi$, $^m\theta$, and $^m\phi$ are the rotations about the ^cx-, ^cy-, and ^cz-axes, respectively. All rotations are defined with respect to the reference frame. Thus, the position of the translator can be described in 6-DOF. The transformation matrix ^mT_c for a

position from the global to the local coordinate system is equal to

$$\begin{aligned}{}^{\mathbf{m}}\mathbf{T}_{\mathbf{c}} = {}^{\mathbf{c}}\mathbf{T}_{\mathbf{m}}{}^{-1} &= \begin{pmatrix} {}^{\mathbf{c}}\mathbf{R}_{\mathbf{m}}{}^{\mathsf{T}} & -{}^{\mathbf{c}}\mathbf{R}_{\mathbf{m}}{}^{\mathsf{T}}{}^{c}\vec{p} \\ 0 & 1 \end{pmatrix} \\ &= \begin{pmatrix} {}^{\mathbf{m}}\mathbf{R}_{\mathbf{c}} & -{}^{\mathbf{m}}\mathbf{R}_{\mathbf{c}}{}^{c}\vec{p} \\ 0 & 1 \end{pmatrix} \end{aligned} \tag{9}$$

because ${}^{\mathbf{m}}\mathbf{T}_{\mathbf{c}}$ is orthonormal.

Applying the appropriate transformation matrix, a position can be transferred between the coordinate systems, according to

$$\begin{aligned} \begin{pmatrix} {}^{m}\vec{x} \\ 1 \end{pmatrix} &= {}^{\mathbf{m}}\mathbf{T}_{\mathbf{c}} \begin{pmatrix} {}^{c}\vec{x} \\ 1 \end{pmatrix} \\ {}^{m}\vec{x} &= {}^{\mathbf{m}}\mathbf{R}_{\mathbf{c}}({}^{c}\vec{x} - {}^{c}\vec{p}) \end{aligned} \tag{10}$$

and a free vector as defined in [8], e.g., the current density, according to

$$\begin{aligned} \begin{pmatrix} {}^{m}\vec{J} \\ 0 \end{pmatrix} &= {}^{\mathbf{m}}\mathbf{T}_{\mathbf{c}} \begin{pmatrix} {}^{c}\vec{J} \\ 0 \end{pmatrix} \\ {}^{m}\vec{J} &= {}^{\mathbf{m}}\mathbf{R}_{\mathbf{c}}{}^{c}\vec{J}. \end{aligned} \tag{11}$$

IV. Magnetic Surface Charge Model

The full analysis of this type of planar actuators cannot be carried out with finite-element simulations. As the flux is not confined in iron, a large and dense mesh is required for accurate force and torque calculations in finite-element analyses. Therefore, only small parts of a planar actuator topology can be simulated. A model which has similarities with boundary-element methods has been developed to simulate large planar actuator topologies in a relatively short time. The permanent magnets are modeled with magnetic surface charges and the force and torque are calculated with the Lorentz force equation. The size of the actuator is unlimited. Because the field of the permanent magnets can be solved analytically, only the volume integral over the coils has to be solved numerically to calculate the force and torque.

A. Magnetic Flux Density

The magnetic field of a cuboidal magnet in three dimensions can be derived from Maxwell's equations. The solution of the Maxwell's equations for the permanent magnet, using a scalar potential, results in a model of the permanent magnet with two surface charges. The surface charges are on the sides of the permanent magnet, which are perpendicular to the magnetization direction. The surface charges $\pm\sigma$ are equal to $\pm B_r$, the remanent magnetization of the permanent magnet. The only assumption made is that the relative permeability $\mu_r = 1$ in and outside the permanent magnet. Fig. 3 shows the model of a magnet, magnetized in the positive ${}^{m}z$-direction. The sizes of the magnet are $2a$, $2b$, and $2c$ in the x-, y-, and z-direction, respectively. The center of the magnet is located at

$${}^{m}\vec{q} = [{}^{m}q_x \quad {}^{m}q_y \quad {}^{m}q_z]^{\mathsf{T}}. \tag{12}$$

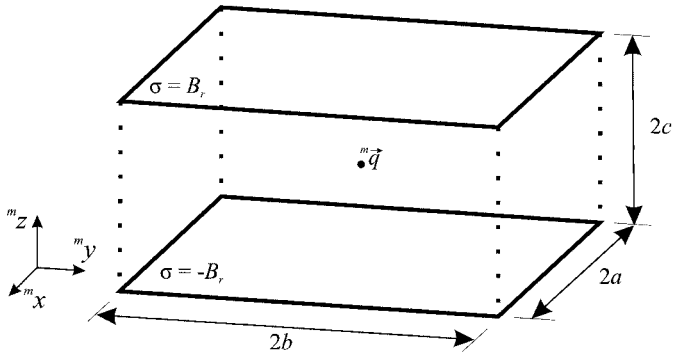

Fig. 3. Charge model of a magnet magnetized in the positive z-direction.

The magnetic flux density in the local coordinate system

$${}^{m}\vec{B} = [{}^{m}B_x \quad {}^{m}B_y \quad {}^{m}B_z]^{\mathsf{T}} \tag{13}$$

of a cuboidal magnet magnetized in the positive z-direction is equal to [9]

$${}^{m}B_x = \frac{B_r}{4\pi}\sum_{i=0}^{1}\sum_{j=0}^{1}\sum_{k=0}^{1}(-1)^{i+j+k}\log(R-T) \tag{14}$$

$${}^{m}B_y = \frac{B_r}{4\pi}\sum_{i=0}^{1}\sum_{j=0}^{1}\sum_{k=0}^{1}(-1)^{i+j+k}\log(R-S) \tag{15}$$

$${}^{m}B_z = \frac{B_r}{4\pi}\sum_{i=0}^{1}\sum_{j=0}^{1}\sum_{k=0}^{1}(-1)^{i+j+k}\operatorname{atan2}\left(\frac{ST}{RU}\right) \tag{16}$$

where $\operatorname{atan2}$ is a four-quadrant arctangent function and

$$R = \sqrt{S^2+T^2+U^2} \tag{17}$$

$$S = ({}^{m}x - {}^{m}q_x) - (-1)^{i}a \tag{18}$$

$$T = ({}^{m}y - {}^{m}q_y) - (-1)^{j}b \tag{19}$$

$$U = ({}^{m}z - {}^{m}q_z) - (-1)^{k}c. \tag{20}$$

The magnetic field of an array of permanent magnets is equal to the sum of the contributions of the individual magnets.

B. Force and Torque

The force and torque can be calculated according to the Lorentz force principle. The force on the translator is opposite to the force on the coils. By applying the coordinate transformations, the translator can be positioned in 6-DOF with respect to the stator. The force on the permanent-magnet array in the local coordinate system is

$${}^{m}\vec{F} = -\int_{V_{\text{coil}}}\left({}^{\mathbf{m}}\mathbf{R}_{\mathbf{c}}{}^{c}\vec{J}({}^{c}\vec{x})\right) \times {}^{m}\vec{B}\left({}^{\mathbf{m}}\mathbf{R}_{\mathbf{c}}({}^{c}\vec{x} - {}^{c}\vec{p})\right)\mathrm{d}^{c}V. \tag{21}$$

The torque in the local coordinate system is equal to

$${}^{m}\vec{T} = -\int_{V_{\text{coil}}}({}^{\mathbf{m}}\mathbf{R}_{\mathbf{c}}({}^{c}\vec{x} - {}^{c}\vec{p})) \times \left(\left({}^{\mathbf{m}}\mathbf{R}_{\mathbf{c}}{}^{c}\vec{J}({}^{c}\vec{x})\right) \times {}^{m}\vec{B}\left({}^{\mathbf{m}}\mathbf{R}_{\mathbf{c}}({}^{c}\vec{x} - {}^{c}\vec{p})\right)\right)\mathrm{d}^{c}V. \tag{22}$$

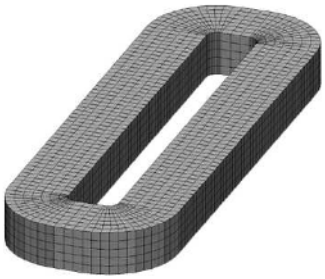

Fig. 4. Mesh of a coil in the magnetic surface charge model.

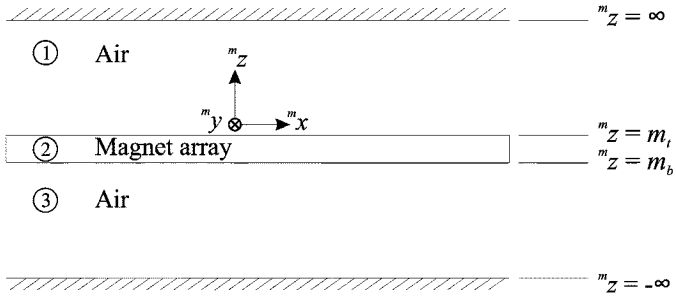

Fig. 5. Problem divided into three regions.

The volume integral is solved numerically using a cuboidal mesh as shown in Fig. 4. In every mesh element the integral is solved with the 3-D trapezoidal rule.

The calculation time of the model, which is implemented in C++, reduces the calculation time from 40 min in a finite-element analysis to approximately 20–30 s for a partial planar actuator model with a Halbach magnet array with 5×5 poles (85 permanent magnets) and three coils. Although the presented model has no size limit, the calculation time is proportional to the number and the size of the coils and the number of permanent magnets.

V. Harmonic Model

The magnetic surface charge model takes into account all the individual magnets in the magnet-array of the planar actuator. Consequently, the simulation time for large planar actuator topologies is relatively long. For the comparison of a large number of topologies and the development and verification of decoupling algorithms, a further reduction of the calculation time is important because the force and torque have to be calculated for many positions of the translator in the xy-plane.

The reduction of the calculation time can be achieved by modeling the permanent magnets as an infinitely large magnet array with Fourier series and by reducing the DOF in the model. This results in two model limitations. First, the edge effects of the magnet array are not included. However, the edge effects are of minor importance in many design steps, such as the optimization of the sizes of the magnets and the coils. Second, the model cannot be used for simulation of the planar actuator system with a controller for all 6-DOF, because the rotational degrees of freedom are fixed.

A. Magnetic Flux Density

The expression of the magnetic flux density of an infinitely large magnet array is derived in the coordinate system of the translator. The magnetization vector function $\vec{M}$ describing the Halbach array which is shown in Fig. 2 can be expressed as Fourier series

$$ {}^m\vec{M} = \frac{B_r}{\mu_0} \sum_{k=1}^{\infty} \sum_{l=1}^{\infty} \begin{bmatrix} -a(k)b(l) \cos\left(\frac{k\pi\, {}^m x}{\tau}\right) \sin\left(\frac{l\pi\, {}^m y}{\tau}\right) \\ -b(k)a(l) \sin\left(\frac{k\pi\, {}^m x}{\tau}\right) \cos\left(\frac{l\pi\, {}^m y}{\tau}\right) \\ b(k)b(l) \sin\left(\frac{k\pi\, {}^m x}{\tau}\right) \sin\left(\frac{l\pi\, {}^m y}{\tau}\right) \end{bmatrix} \tag{23} $$

where k and l are the harmonic numbers for the x- and y-direction, respectively, and

$$ a(k) = \frac{4}{k\pi} \cos\left(\frac{k\tau_m\pi}{2\tau}\right) \sin\left(\frac{k\pi}{2}\right) \tag{24} $$

$$ b(k) = \frac{4}{k\pi} \sin\left(\frac{k\tau_m\pi}{2\tau}\right) \sin\left(\frac{k\pi}{2}\right) \tag{25} $$

where τ is the pole pitch and τ_m is the length of the side of the magnets which are magnetized in the ${}^mz$-direction (see also Fig. 2).

To solve the field equations, the problem is split into three regions. The regions are shown in Fig. 5. Regions 1 and 3 are in air and region 2 contains the permanent magnets. The empty spaces in the magnet array are assumed to consist of material with the same relative permeability as the permanent magnets. Although in reality these empty spaces will be filled with air or an epoxy resin, the error is small because modern NdFeB permanent magnets have a relative permeability of 1.03–1.05.

In regions 1 and 3, the next equations apply (only the equations for region 1 are shown)

$$ \nabla \times {}^m\vec{H}_1 = \vec{0} \tag{26} $$

$$ {}^m\vec{B}_1 = \mu_0\, {}^m\vec{H}_1 \tag{27} $$

$$ \nabla \cdot {}^m\vec{B}_1 = 0 \tag{28} $$

where ${}^m\vec{B}_1$ is the magnetic flux density, ${}^m\vec{H}_1$ is the magnetic field strength, and the subscript denotes the region. A scalar potential ${}^m\Psi_1$ is introduced accordingly:

$$ {}^m\vec{H}_1 = -\nabla\, {}^m\Psi_1. \tag{29} $$

After substitution of the scalar potential in (26)–(28), the following three-dimensional Laplace equation is obtained:

$$ \nabla^2\, {}^m\Psi_1 = 0. \tag{30} $$

Region 2 is the area with the magnets. In the magnets

$$ \nabla \times {}^m\vec{H}_2 = \vec{0} \tag{31} $$

$$ {}^m\vec{B}_2 = \mu_0\mu_r\, {}^m\vec{H}_2 + \mu_0\, {}^m\vec{M} \tag{32} $$

$$ \nabla \cdot {}^m\vec{B}_2 = 0 \tag{33} $$

where μ_r is the relative permeability of the magnets. A scalar potential ${}^m\Psi_2$ is introduced accordingly:

$$ {}^m\vec{H}_2 = -\nabla\, {}^m\Psi_2. \tag{34} $$

After substitution of the scalar potential in (31)–(33), the following equation is obtained:

$$\nabla^2\,{}^m\Psi_2 = \nabla\cdot\frac{{}^m\vec{M}}{\mu_r} = \frac{B_r}{\mu_0\mu_r}\sum_{k=1}^{\infty}\sum_{l=1}^{\infty}\left(\frac{a(k)b(l)k\pi + b(k)a(l)l\pi}{\tau}\right)\cdot\sin\left(\frac{k\pi\,{}^m x}{\tau}\right)\sin\left(\frac{l\pi\,{}^m y}{\tau}\right). \quad (35)$$

At infinite distance from the magnet array

$${}^m\Psi_1({}^m z=\infty) = 0 \quad (36)$$

$${}^m\Psi_3({}^m z=-\infty) = 0. \quad (37)$$

The following boundary conditions apply on the interface between the magnets and the air:

$${}^mH_{1x}({}^m z=m_t) = {}^mH_{2x}({}^m z=m_t) \quad (38)$$

$${}^mH_{1y}({}^m z=m_t) = {}^mH_{2y}({}^m z=m_t) \quad (39)$$

$${}^mB_{1z}({}^m z=m_t) = {}^mB_{2z}({}^m z=m_t) \quad (40)$$

$${}^mH_{2x}({}^m z=m_b) = {}^mH_{3x}({}^m z=m_b) \quad (41)$$

$${}^mH_{2y}({}^m z=m_b) = {}^mH_{3y}({}^m z=m_b) \quad (42)$$

$${}^mB_{2z}({}^m z=m_b) = {}^mB_{3z}({}^m z=m_b) \quad (43)$$

where $m_t - m_b$ is the height of the magnet array.

The Laplace equations can be solved with the method of separation of variables, i.e., the solution of the scalar potential is a product of functions which involve only one variable. For this particular problem, a solution of the form

$${}^m\Psi = \sum_{k=1}^{\infty}\sum_{l=1}^{\infty} Z({}^m z)\sin\left(\frac{k\pi^m x}{\tau}\right)\sin\left(\frac{l\pi^m y}{\tau}\right) \quad (44)$$

is substituted. In regions 1 and 3, substitution of (44) in (30) results in

$$-\sin\left(\frac{k\pi^m x}{\tau}\right)\sin\left(\frac{l\pi^m y}{\tau}\right)\cdot\left(\frac{\mathrm{d}^2 Z({}^m z)}{\mathrm{d}^m z^2} - \lambda^2 Z({}^m z)\right) = 0 \quad (45)$$

where

$$\lambda = \sqrt{\left(\frac{k\pi}{\tau}\right)^2 + \left(\frac{l\pi}{\tau}\right)^2}. \quad (46)$$

The general solution of this equation is

$$Z({}^m z) = K_1 e^{-\lambda^m z} + K_3 e^{\lambda^m z} \quad (47)$$

where K_1 and K_3 are constants. Because of the boundary conditions (zero scalar potential for $z = \pm\infty$)

$${}^m\Psi_1 = \sum_{k=1}^{\infty}\sum_{l=1}^{\infty} K_1 e^{-\lambda^m z}\sin\left(\frac{k\pi^m x}{\tau}\right)\sin\left(\frac{l\pi^m y}{\tau}\right) \quad (48)$$

and

$${}^m\Psi_3 = \sum_{k=1}^{\infty}\sum_{l=1}^{\infty} K_3 e^{\lambda^m z}\sin\left(\frac{k\pi^m x}{\tau}\right)\sin\left(\frac{l\pi^m y}{\tau}\right). \quad (49)$$

In region 2, a nonhomogeneous differential equation is obtained

$$-\sin\left(\frac{n\pi^m x}{\tau}\right)\sin\left(\frac{m\pi^m y}{\tau}\right)\cdot\left(\frac{\mathrm{d}^2 Z({}^m z)}{\mathrm{d}^m z^2} - \lambda^2 Z({}^m z)\right) = \frac{B_r}{\mu_0\mu_r}\left(\frac{a(k)b(l)k\pi}{\tau} + \frac{b(k)a(l)l\pi}{\tau}\right)\cdot\sin\left(\frac{k\pi^m x}{\tau}\right)\sin\left(\frac{l\pi^m y}{\tau}\right). \quad (50)$$

The solution is

$$Z({}^m z) = K_{21}e^{-\lambda^m z} + K_{22}e^{\lambda^m z} - \frac{B_r a(l)b(k)m\tau + B_r a(k)b(l)n\tau}{\mu_0\mu_r\pi(k^2+l^2)} \quad (51)$$

where K_{21} and K_{22} are constants.

The constants K_1, K_{21}, K_{22}, and K_3 can be calculated with the boundary conditions. The resulting expression for the magnetic flux density distribution in the area of interest, region 3, is expressed in the local coordinate system

$${}^m\vec{B}_3({}^m\vec{x}) = -\mu_0\nabla^m\Psi_3 = -\mu_0\sum_{k=1}^{\infty}\sum_{l=1}^{\infty} K_3 e^{\lambda^m z}\cdot\begin{bmatrix}\frac{k\pi}{\tau}\cos\left(\frac{k\pi^m x}{\tau}\right)\sin\left(\frac{l\pi^m y}{\tau}\right)\\ \frac{l\pi}{\tau}\sin\left(\frac{k\pi^m x}{\tau}\right)\cos\left(\frac{l\pi^m y}{\tau}\right)\\ \lambda\sin\left(\frac{k\pi^m x}{\tau}\right)\sin\left(\frac{l\pi^m y}{\tau}\right)\end{bmatrix} \quad (52)$$

where for $\mu_r = 1$

$$K_3 = B_r\left(e^{-m_t\lambda} - e^{-m_b\lambda}\right)\cdot\frac{\left(b(k)b(l)\pi\left(k^2+l^2\right) + a(k)b(l)k\lambda\tau + a(l)b(k)l\lambda\tau\right)}{2\left(k^2+l^2\right)\pi\lambda\mu_0}. \quad (53)$$

B. Force and Torque

The obtained magnetic flux density distribution can be substituted in (21) and (22). In that case, the calculation speed is increased because it is no longer dependent on the number of magnets in the magnet array. However, the calculation speed can be increased further by reducing the rotational degrees-of-freedom in the model. i.e., ${}^m\psi = 0$ rad, ${}^m\theta = 0$ rad and ${}^m\phi = 0$ rad or ${}^m\phi = \pm\frac{\pi}{4}$ rad.

For convenience, (52) is rewritten as

$${}^m\vec{B}_3({}^m\vec{x}) = \sum_{k=1}^{\infty}\sum_{l=1}^{\infty} e^{(\lambda^m z)}\,{}^m\vec{B}_{3xy}({}^m\vec{x},k,l) \quad (54)$$

where

$${}^m\vec{B}_{3xy}({}^m\vec{x},k,l) = -\mu_0 K_3\begin{bmatrix}\frac{k\pi}{\tau}\cos\left(\frac{k\pi^m x}{\tau}\right)\sin\left(\frac{l\pi^m y}{\tau}\right)\\ \frac{l\pi}{\tau}\sin\left(\frac{k\pi^m x}{\tau}\right)\cos\left(\frac{l\pi\lambda^m y}{\tau}\right)\\ \sin\left(\frac{k\pi^m x}{\tau}\right)\sin\left(\frac{l\pi^m y}{\tau}\right)\end{bmatrix}. \quad (55)$$

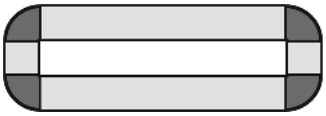

Fig. 6. Coil split into four straight (light gray) and four corner (dark gray) segments.

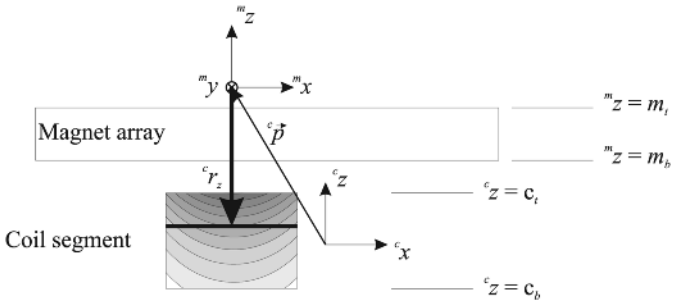

Fig. 7. Effective force arm in the z-direction.

The Lorentz force volume integral can be split into an integral over ${}^{c}z$ and a surface integral over ${}^{c}x$ and ${}^{c}y$

$$
\begin{aligned}
{}^{c}\vec{F} = &-\sum_{k=1}^{\infty}\sum_{l=1}^{\infty} \\
&\int_{V_{\mathrm{Coil}}} {}^{c}\vec{J} \times {}^{\mathbf{c}}\mathbf{R}_{\mathbf{m}}\, {}^{m}\vec{B}_3\left({}^{\mathbf{m}}\mathbf{R}_{\mathbf{c}}({}^{c}\vec{x} - {}^{c}\vec{p})\right) \mathrm{d}^{c}V \\
&= -\sum_{k=1}^{\infty}\sum_{l=1}^{\infty} \int e^{\lambda({}^{c}z - {}^{c}p_z)} \mathrm{d}^{c}z \\
&\cdot \iint {}^{c}\vec{J} \times {}^{\mathbf{c}}\mathbf{R}_{\mathbf{m}}\, {}^{m}\vec{B}_{3xy} \times ({}^{\mathbf{m}}\mathbf{R}_{\mathbf{c}}({}^{c}\vec{x} - {}^{c}\vec{p}), k, l)\, \mathrm{d}^{c}x \mathrm{d}^{c}y.
\end{aligned} \tag{56}
$$

The integral over ${}^{c}z$ can be solved analytically. The surface integral over ${}^{c}x$ and ${}^{c}y$ can be solved analytically in the straight segments of the coil and numerically in the corner segments of the coil. The segments are shown in Fig. 6.

The same approach is applied to the torque. The distribution of the force in the volume of the coil has to be taken into account, when the torque is calculated. If the volume integral for the torque is also split, then this information might be lost in the ${}^{c}z$-direction. Because the magnetic flux density decays with an exponential function in the z-direction, an effective attaching point of the force in the coil in the z-direction ${}^{c}r_z$, can be calculated, accordingly:

$$
\int_{c_b}^{c_t} ({}^{c}z - {}^{c}p_z)\, e^{\lambda({}^{c}z - {}^{c}p_z)} \mathrm{d}^{c}z = {}^{c}r_z \int_{c_b}^{c_t} e^{\lambda({}^{c}z - {}^{c}p_z)} \mathrm{d}^{c}z. \tag{57}
$$

The effective arm is then equal to

$$
{}^{c}r_z = c_t - {}^{c}p_z - \frac{1}{\lambda} - \frac{(c_b - c_t)e^{\lambda c_b}}{e^{\lambda c_b} - e^{\lambda c_t}}. \tag{58}
$$

This is also illustrated in Fig. 7. In the cross section of the coil, the magnetic flux density distribution is shown. The highest values of the magnetic flux density and the force (dark gray)

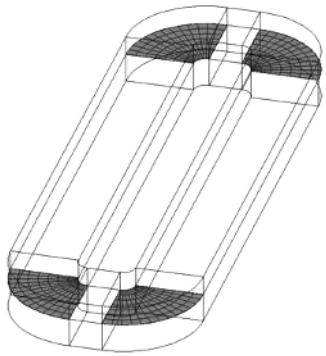

Fig. 8. Mesh of the coil in the harmonic model.

are near the magnet array. The arm ${}^{c}r_z$ for the first harmonic, $k = l = 1$, is shown with the bold arrow and the effective attaching point of the force is indicated with the line in the coil segment.

With the introduction of ${}^{c}r_z$, the volume integral to calculate the torque can also be split into an integral over ${}^{c}z$ and a surface integral over ${}^{c}x$ and ${}^{c}y$

$$
\begin{aligned}
{}^{c}\vec{T} = &-\sum_{k=1}^{\infty}\sum_{l=1}^{\infty} \int_{V_{\mathrm{coil}}} ({}^{c}\vec{x} - {}^{c}\vec{p}) \\
&\times \left({}^{c}\vec{J} \times {}^{\mathbf{c}}\mathbf{R}_{\mathbf{m}}\, {}^{m}\vec{B}_3\left({}^{\mathbf{m}}\mathbf{R}_{\mathbf{c}}({}^{c}\vec{x} - {}^{c}\vec{p})\right)\right) \mathrm{d}^{c}V \\
= &-\sum_{k=1}^{\infty}\sum_{l=1}^{\infty} \int e^{\lambda({}^{c}z - {}^{c}p_z)} \mathrm{d}^{c}z \int\int \begin{bmatrix} {}^{c}x - {}^{c}p_x \\ {}^{c}y - {}^{c}p_y \\ {}^{c}r_z \end{bmatrix} \\
&\times \left({}^{c}\vec{J} \times {}^{\mathbf{c}}\mathbf{R}_{\mathbf{m}}\, {}^{m}\vec{B}_{3xy}\left({}^{\mathbf{m}}\mathbf{R}_{\mathbf{c}}({}^{c}\vec{x} - {}^{c}\vec{p}), k, l\right) \mathrm{d}^{c}x \mathrm{d}^{c}y\right).
\end{aligned} \tag{59}
$$

Also in this case, the integral over ${}^{c}z$ can be solved analytically in all coil segments. The surface integral over ${}^{c}x$ and ${}^{c}y$ can be solved analytically in the straight segments of the coil and numerically in the corner segments of the coil.

The force and torque exerted by a coil on the magnet array of the planar actuator can be calculated for the most part analytically when the rotation angles ${}^{m}\psi = 0$ rad, ${}^{m}\theta = 0$ rad and ${}^{m}\phi = 0$ rad, or ${}^{m}\phi = \pm(\pi/4)$ rad. Only a surface integral has to be solved numerically in the corner segments of the coil as shown in Fig. 8. The calculation time for a planar actuator as shown in Fig. 1 can be reduced to 0.1–1 s, depending on the number of harmonics which are taken into account. This calculation time is convenient to predict the force and torque in a planar actuator at a large number of translator locations, to compare topologies and to test decoupling algorithms.

VI. Analytical Model

The commutation algorithm of the planar actuator has to decouple the force and torque and the coil currents [4]. Therefore, the algorithm needs a model of the force and torque in the actuator as function of all 6-DOF. Although such a model can be calculated with the magnetic surface charge model and stored in a large look-up table, a model-based control and commutation algorithm is preferred. Moreover, an analytical model gives insight in the force and torque production in the actuator.

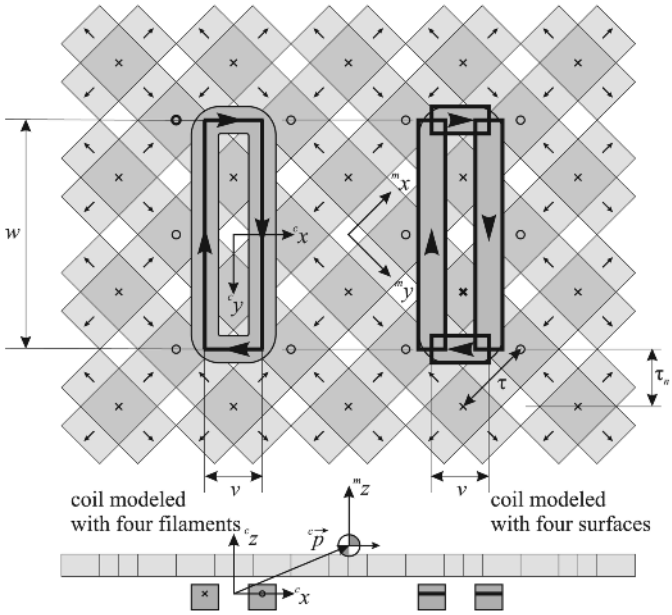

Fig. 9. Coil model with filaments (left) and with surfaces (right).

A. Magnetic Flux Density

The analytical model is derived from the harmonic model by taking into account the first harmonic of the magnetic flux density distribution of the permanent magnet array. The magnetic flux density expression is simplified to

$$ {}^{m}\vec{B}_3({}^{m}\vec{x}) = e^{\lambda\, {}^{m}z} \begin{bmatrix} B_{xy}\cos\left(\frac{\pi\, {}^{m}x}{\tau}\right)\sin\left(\frac{\pi\, {}^{m}y}{\tau}\right) \\ B_{xy}\sin\left(\frac{\pi\, {}^{m}x}{\tau}\right)\cos\left(\frac{\pi\, {}^{m}y}{\tau}\right) \\ B_z\sin\left(\frac{\pi\, {}^{m}x}{\tau}\right)\sin\left(\frac{\pi\, {}^{m}y}{\tau}\right) \end{bmatrix} \tag{60} $$

where $\lambda = (\sqrt{2}\pi/\tau)$ and B_{xy} and B_z are the effective amplitudes of the first harmonic of the flux density distribution at ${}^{m}z = 0$. Transformation of this expression into the global coordinate system of the coils

$$ {}^{c}\vec{B}_3({}^{c}\vec{x}, {}^{c}\vec{p}) = {}^{\mathbf{c}}\mathbf{R}_{\mathbf{m}}\, {}^{m}\vec{B}_3\left({}^{\mathbf{m}}\mathbf{R}_{\mathbf{c}}({}^{c}\vec{x} - {}^{c}\vec{p})\right) \tag{61} $$

results (for ${}^{m}\phi = -\pi/4$ rad and ${}^{m}\psi = {}^{m}\theta = 0$ rad) in

$$ {}^{c}\vec{B}_3({}^{c}\vec{x}, \vec{0}) = \begin{bmatrix} \frac{B_{xy}}{\sqrt{2}} e^{\lambda\, {}^{c}z}\sin\left(\frac{{}^{c}x\sqrt{2}\pi}{\tau}\right) \\ -\frac{B_{xy}}{\sqrt{2}} e^{\lambda\, {}^{c}z}\sin\left(\frac{{}^{c}y\sqrt{2}\pi}{\tau}\right) \\ -\frac{1}{2}B_z e^{\lambda\, {}^{c}z}\left(\cos\left(\frac{{}^{c}x\sqrt{2}\pi}{\tau}\right) - \cos\left(\frac{{}^{c}y\sqrt{2}\pi}{\tau}\right)\right) \end{bmatrix}. \tag{62} $$

Because the mechanical clearance between the translator and the stator will be small, the rotation angles are limited. The rotation angles can be taken into account with Taylor-expansion for the angles ${}^{m}\psi$, ${}^{m}\theta$, and ${}^{m}\phi$. Because ${}^{m}\phi = -\pi/4$, a new pole pitch τ_n can be introduced:

$$ \tau_n = \frac{\tau}{\sqrt{2}}. \tag{63} $$

B. Force and Torque

Because the real-time commutation algorithm is evaluated every sample time, simple expressions for the force and torque are required to reduce the computation time of the model and to reduce the load on the DSP in the control hardware of the actuator. Therefore, the coil is modeled with four straight filaments, as shown in Fig. 9. The filaments are located in the middle of the conductors. In the ${}^{c}z$-direction, they are located at the effective attaching point of the force. The Lorentz force can be calculated by solving a line integral. The force exerted on the translator ${}^{c}\vec{F} = [{}^{c}F_x\ {}^{c}F_y\ {}^{c}F_z]^{\mathsf{T}}$, expressed in the global coordinate system, by one coil, which center is located at $({}^{c}x\ {}^{c}y\ 0)$, is

$$ \begin{aligned} {}^{c}\vec{F} &= -\oint_C {}^{c}\vec{J} \times {}^{c}\vec{B}_3 \mathrm{d}l \\ &= -\int_{{}^{c}x-v/2}^{{}^{c}x+v/2} [I \quad 0 \quad 0]^{\mathsf{T}} \\ &\quad \times {}^{c}\vec{B}_3([{}^{c}x' \quad {}^{c}y - w/2 \quad 0], {}^{c}\vec{p})\mathrm{d}{}^{c}x' \\ &\quad - \int_{{}^{c}y-w/2}^{{}^{c}y+w/2} [0 \quad I \quad 0]^{\mathsf{T}} \\ &\quad \times {}^{c}\vec{B}_3([{}^{c}x + v/2 \quad {}^{c}y' \quad 0], {}^{c}\vec{p})\mathrm{d}{}^{c}y' \\ &\quad - \int_{{}^{c}x-v/2}^{{}^{c}x+v/2} [-I \quad 0 \quad 0]^{\mathsf{T}} \\ &\quad \times {}^{c}\vec{B}_3([{}^{c}x' \quad {}^{c}y + w/2 \quad 0], {}^{c}\vec{p})\mathrm{d}{}^{c}x' \\ &\quad - \int_{{}^{c}y-w/2}^{{}^{c}y+w/2} [0 \quad -I \quad 0]^{\mathsf{T}} \\ &\quad \times {}^{c}\vec{B}_3([{}^{c}x - v/2 \quad {}^{c}y' \quad 0], {}^{c}\vec{p})\mathrm{d}{}^{c}y' \end{aligned} \tag{64} $$

where v and w are the sizes of the filament coil along the ${}^{c}x$- and ${}^{c}y$-directions, respectively, and I is the current through the coil in Ampere-turns.

The torque exerted on the translator ${}^{c}\vec{T} = [{}^{c}T_x\ {}^{c}T_y\ {}^{c}T_z]^{\mathsf{T}}$, expressed in the global coordinate system, is

$$ \begin{aligned} {}^{c}\vec{T} &= -\oint_C ({}^{c}\vec{x} - {}^{c}\vec{p}) \times \left({}^{c}\vec{J} \times {}^{c}\vec{B}_3\right) \mathrm{d}l \\ &= -\int_{{}^{c}x-v/2}^{{}^{c}x+v/2} ({}^{c}\vec{x} - {}^{c}\vec{p}) \times ([I \quad 0 \quad 0]^{\mathsf{T}} \\ &\quad \times {}^{c}\vec{B}_3([{}^{c}x' \quad {}^{c}y - w/2 \quad 0]^{\mathsf{T}}, {}^{c}\vec{p}))\mathrm{d}{}^{c}x' \\ &\quad - \int_{{}^{c}y-w/2}^{{}^{c}y+w/2} ({}^{c}\vec{x} - {}^{c}\vec{p}) \times ([0 \quad I \quad 0]^{\mathsf{T}} \\ &\quad \times {}^{c}\vec{B}_3([{}^{c}x + v/2 \quad {}^{c}y' \quad 0]^{\mathsf{T}}, {}^{c}\vec{p}))\mathrm{d}{}^{c}y' \\ &\quad - \int_{{}^{c}x-v/2}^{{}^{c}x+v/2} ({}^{c}\vec{x} - {}^{c}\vec{p}) \times ([-I \quad 0 \quad 0]^{\mathsf{T}} \\ &\quad \times {}^{c}\vec{B}_3([{}^{c}x' \quad {}^{c}y + w/2 \quad 0]^{\mathsf{T}}, {}^{c}\vec{p}))\mathrm{d}{}^{c}x' \\ &\quad - \int_{{}^{c}y-w/2}^{{}^{c}y+w/2} ({}^{c}\vec{x} - {}^{c}\vec{p}) \times ([0 \quad -I \quad 0]^{\mathsf{T}} \\ &\quad \times {}^{c}\vec{B}_3([{}^{c}x - v/2 \quad {}^{c}y' \quad 0]^{\mathsf{T}}, {}^{c}\vec{p}))\mathrm{d}{}^{c}y'. \end{aligned} \tag{65} $$

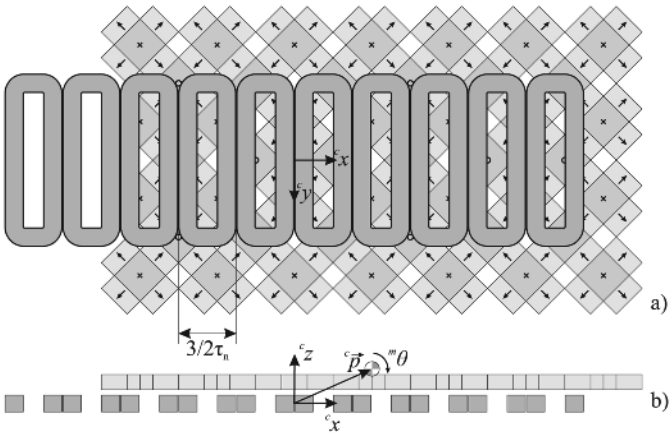

Fig. 10. Bottom (a) and side view (b) of the 3-DOF actuator.

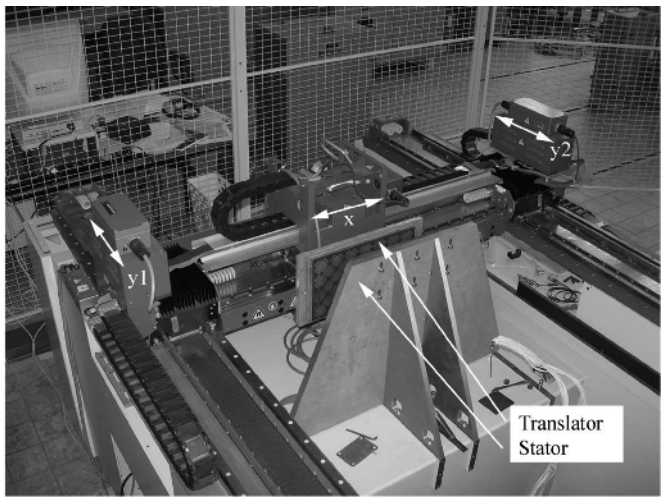

Fig. 11. Measurement setup. The 3-DOF actuator is put on its side and attached to an xy-positioning system with three linear motors (x, $y1$, and $y2$).

If the width of the coil $w = 2n\tau_n$, where n is an integer, and if ${}^m\phi = -\pi/4$ rad and ${}^m\psi = {}^m\theta = 0$ rad, the coil only produces force in the ${}^cx$- and ${}^cz$-directions. The force and torque expressions for such a coil with $v = \tau_n$ and $w = 4\tau_n$ are

$$ {}^c\vec{F} = \begin{bmatrix} 2\sqrt{2}B_z I\tau \exp\left(-\lambda {}^cp_z\right)\sin\left(\frac{\sqrt{2}\pi({}^cp_x - {}^cx)}{\tau}\right) \\ 0 \\ 4B_{xy} I\tau \exp\left(-\lambda {}^cp_z\right)\cos\left(\frac{\sqrt{2}\pi({}^cp_x - {}^cx)}{\tau}\right) \end{bmatrix} \tag{66} $$

$$ {}^c\vec{T} = \begin{bmatrix} \left(\begin{array}{c} ({}^cy - {}^cp_y)\,{}^cF_z + \\ \sqrt{2}B_{xy} I\tau^2 \exp\left(-\lambda {}^cp_z\right)\sin\left(\frac{\sqrt{2}\pi({}^cp_y - {}^cy)}{\tau}\right) \end{array} \right) \\ ({}^cp_x - {}^cx)\,{}^cF_z - {}^cp_z\,{}^cF_x \\ {}^cF_x\,({}^cp_y - {}^cy) \end{bmatrix}. \tag{67} $$

The force components in the ${}^cx$- and ${}^cz$-directions are 90° out of phase as expected in this type of actuator. Equation (67) shows that the torque, i.e., component ${}^cT_x$, cannot be expressed as an arm multiplied by a force. Therefore, a single attaching point of the force cannot be defined and the distribution of the force over the coil should indeed be taken into account.

The accuracy of the analytical model can be improved by modeling the coil by four surfaces instead of four filaments, as shown in Fig. 9. Modeling the coil with four surfaces results in a similar model comparable to (66) and (67), except for the ${}^cT_y$ term. ${}^cT_y$ has a small extra term which is proportional to ${}^cF_x$. The use of the model with the four surfaces instead of the four filaments in the commutation algorithm of planar actuators reduces the cross-talk of the force and torque, especially for 6-DOF planar actuators with a low mass center point.

VII. Experiments

The magnetic surface charge model, the harmonic model, and the analytical model have been verified on a 3-DOF linear actuator with moving magnets. This coreless actuator [10], is a pre-prototype for a 6-DOF planar actuator and was manufactured for the verification of the electromechanical models and the commutation method [4]. An overview of the 3-DOF actuator is shown in Fig. 10. The degrees of freedom which can be actuated are levitation (${}^cz$-direction), propulsion (${}^cx$-direction), and rotation (${}^m\theta$-angle) of the translator. The other degrees of freedom have to be supported with an external bearing system.

The stator of the actuator consists of 10 coils which are connected to single-phase power amplifiers. The coils are displaced 270 electrical degrees, according to a semi-four-phase system. To reduce the damping force due to eddy currents in the aluminum construction, the coils are attached to an aluminum nitrite (AlN) plate. This ceramic material has a low electrical conductivity but a high thermal conductivity.

The translator of the actuator is a Halbach magnet array, which is glued to an aluminum plate. The rectangular magnets, which are magnetized in the xy-plane, are half the size of the square magnets, i.e., $\tau_m/\tau = 2/3$. As a result, the magnetic flux distribution does not contain a third harmonic component, which can be derived with the harmonic model. This results in a strong reduction of the force ripples.

The presented models were verified by measuring the force and torque on the translator. To position the translator of the 3-DOF actuator with respect to its stator, the translator was attached to an xy-positioning system with three linear motors. This positioning system or H-drive is shown in Fig. 11. The H-drive consists of three linear motors. Between the $y1$- and $y2$-motors, a third linear motor (x) is mounted. Because the coupling between the $y1$- and $y2$-motors is not rigid, the x-motor can slightly rotate. By attaching the 3-DOF actuator on its side, the degrees-of-freedom of both the 3-DOF actuator and the H-drive match. A 6-DOF load cell (JR3 45E15A4-I63-S 100N10) was mounted between the 3-DOF actuator and the x-motor of the H-drive to measure the force and the torque exerted on the translator. This is shown in Fig. 12.

The force and torque were measured while one coil was supplied with a direct current of 1 A and the translator was moved along the coil at a speed of 0.02 m/s. Because the bandwidth of the sensor was much higher than the bandwidth of the controllers of the H-drive, the measurement data was filtered off-line with a high order anti-causal low-pass filter with a cut-off

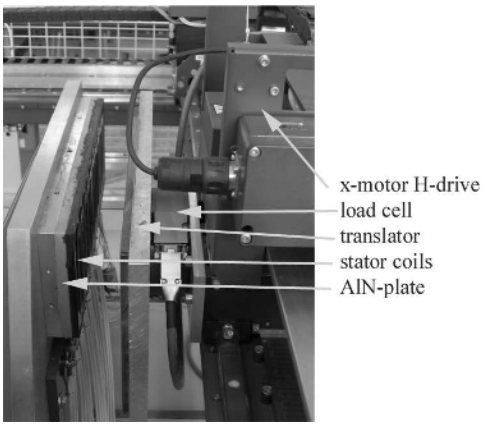

Fig. 12. Detail of the measurement setup.

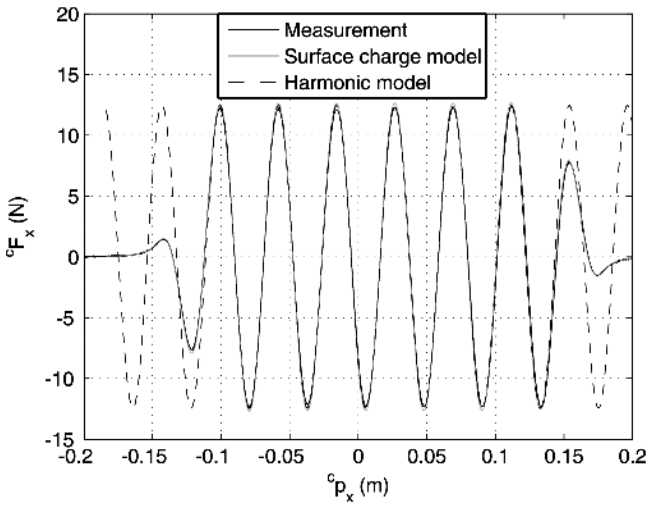

Fig. 13. Measurement and prediction of ${}^cF_x$. Mechanical clearance: 1 mm.

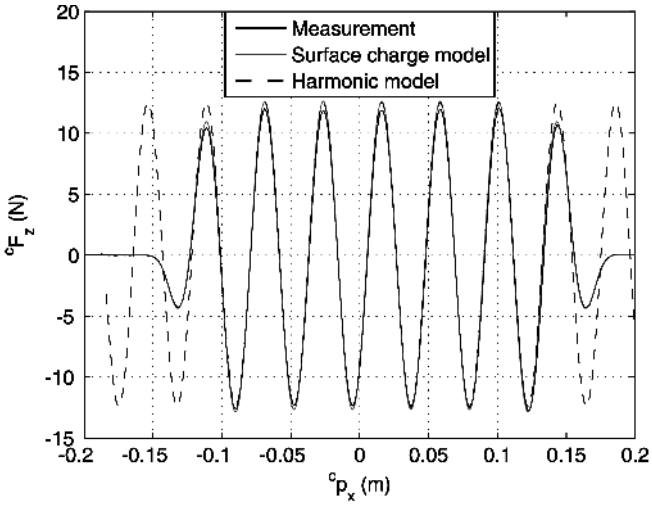

Fig. 14. Measurement and prediction of ${}^cF_z$. Mechanical clearance: 1 mm.

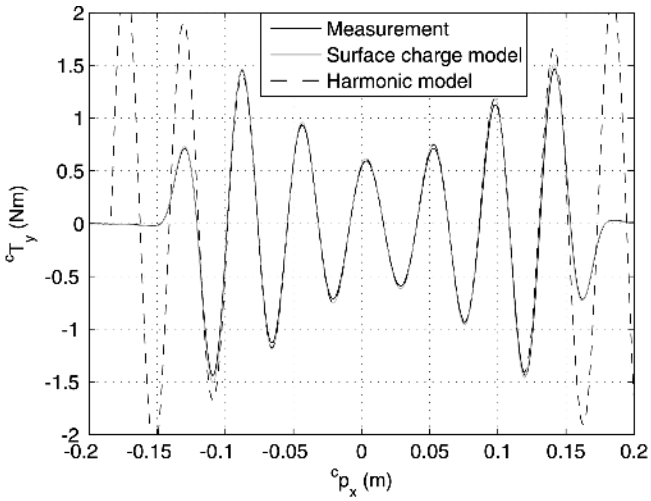

Fig. 15. Measurement and prediction of ${}^cT_y$. Mechanical clearance: 1 mm.

frequency of 25 Hz. Consequently, high frequency disturbances of the H-drive are removed from the measurement signals. Because of the low measurement speed in comparison with the pole pitch ($\tau_n = 21.21$ mm), the higher harmonics of the force and torque are not suppressed by the filter.

Figs. 13, 14, and 15 show the predicted and measured force ${}^cF_x$ and ${}^cF_z$, and torque ${}^cT_y$, respectively. The mechanical clearance between the stator and translator was 1 mm and ${}^m\theta = 0$ rad. Because the harmonic model assumes an infinitely long translator, the end-effects of the magnet array are only predicted by the surface charge model. Fig. 16 shows a detail of the ${}^cF_x$ waveform. The surface charge model predicts a larger force than the harmonic model because the permanent magnets are modeled with a relative permeability equal to 1, while the permeability of the used permanent magnets was equal to 1.03. The predictions are in good agreement with the measurements.

The figures do not show the predictions of the analytical model because the differences between the predictions of the harmonic model and the analytical model are very small. These differences are shown in Fig. 17. For this actuator, the analytical

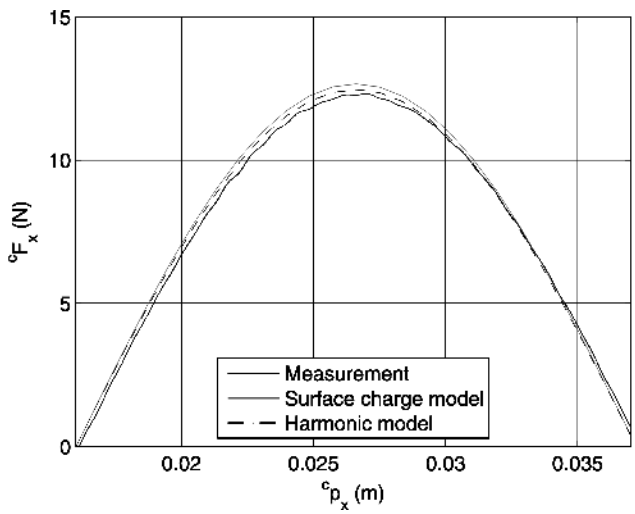

Fig. 16. Detail of the measurement and prediction of ${}^cF_x$.

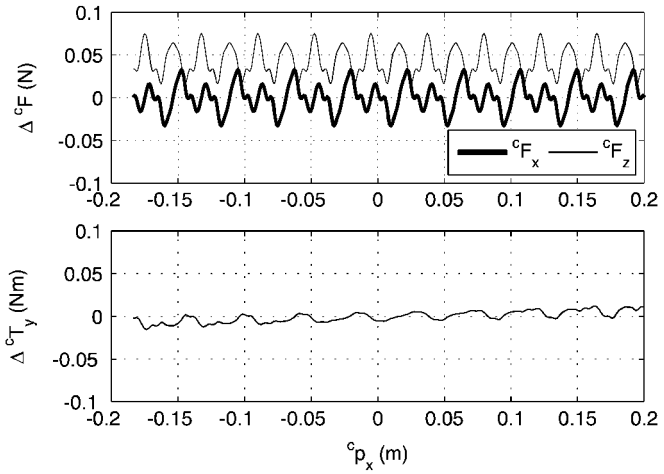

Fig. 17. Difference of the predictions of the harmonic and the analytical model.

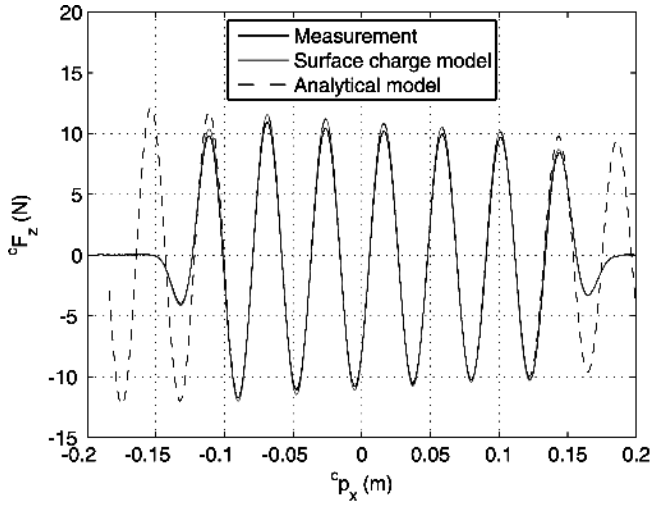

Fig. 18. Measurement and prediction of ${}^{c}F_z$. Minimal mechanical clearance: 0.9 mm and ${}^{m}\theta = 5$ mrad.

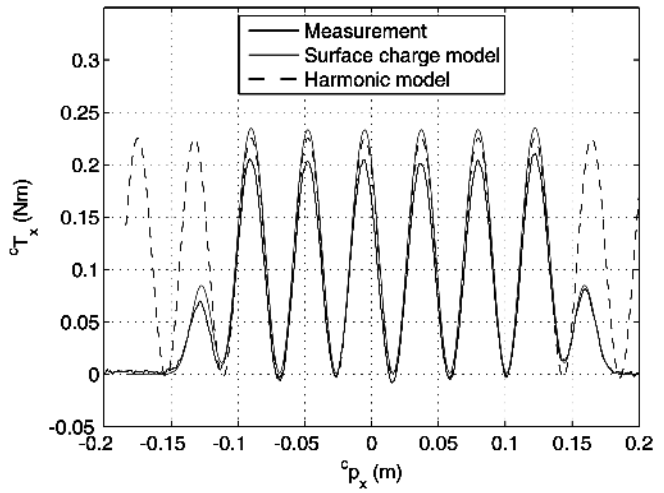

Fig. 19. Measurement and prediction of ${}^{c}T_x$. Mechanical clearance: 2 mm and ${}^{c}p_y - {}^{c}y = \tau_n/2$.

model is an accurate and a computational inexpensive substitute for the harmonic model.

The force component ${}^{c}F_z$ is shown in Fig. 18 when the translator is rotated 5 mrad. The force can be accurately predicted with the surface charge model and with the analytical model with Taylor expansion for the angle.

The analytical model predicts a term in the torque component ${}^{c}T_x$ which cannot be expressed in the derived force components. In the 3-DOF actuator this term is absent because ${}^{c}p_y - {}^{c}y = 0$. However, to validate the model ${}^{c}T_x$ was measured with ${}^{c}p_y - {}^{c}y = \tau_n/2$. The mechanical clearance between the stator and translator was 2 mm and ${}^{m}\theta = 0$ rad. Fig. 19 shows the measured and predicted torque offset clearly and confirms that the distribution of the force over the coil should be taken into account in the torque calculation in planar actuators.

VIII. Conclusion

Three methods to predict the force and torque in a 6-DOF moving-magnet planar actuator are presented. Because of the absence of iron, the force and torque are calculated with the Lorentz force law. The magnetic surface charge method is the most computational expensive model because it models all permanent magnets on the translator separately. By neglecting the end-effects of the permanent-magnet array and reducing the degrees-of-freedom in the model, the force and torque can be calculated for the most part analytically with the harmonic model. Because only four surfaces in the corners of the coil are meshed, the computation time is low. Finally, a fully analytical model is presented which can be evaluated in real-time by the controller of a planar actuator. The predicted force and torque are in good agreement with the measurements on a 3-DOF moving-magnet actuator. All models can be easily modified for moving-coil planar actuators and coreless linear actuators.

Acknowledgment

This IOP-EMVT project was funded by SenterNovem. SenterNovem is an agency of the Dutch Ministry of Economical Affairs. The authors would like to thank M. Uyt De Willigen for his assistance with the experiments. The authors would also like to thank ASML, Assembléon, Philips Applied Technologies, Prodrive, and Tecnotion for their valuable contributions and support.

References

[1] W. J. Kim, D. L. Trumper, and J. H. Lang, "Modeling and vector control of a planar magnetic levitator," *IEEE Trans. Ind. Appl.*, vol. 34, no. 6, pp. 1254–1262, Nov./Dec. 1998.

[2] A. J. Hazelton, M. B. Binnard, and J. M. Gery, "Electric Motors and Positioning Devices Having Moving Magnet Arrays and Six Degrees of Freedom," U.S. Patent 6 208 045 327, 2001.

[3] J. C. Compter, "Electro-dynamic planar motor," *Precision Eng.*, vol. 28, no. 2, pp. 171–180, Apr. 2004.

[4] C. M. M. van Lierop, J. W. Jansen, A. A. H. Damen, and P. P. J. van den Bosch, "Control of multi-degree-of-freedom planar actuators," in *Proc. 2006 IEEE Int. Conf. Control Application*, Munich, Germany, Oct. 2006, pp. 2516–2521.

[5] J. C. Compter, "A planar motor with electro-dynamic propulsion and levitation under 6-dof control," in *Proc. 4th Int. Symp. Linear Drives for Industrial Applications*, Birmingham, U.K., Sep. 2003, pp. 149–152.

[6] D. L. T. W. J. Kim and M. E. Williams, "Design and analysis framework for linear permanent-magnet machines," *IEEE Trans. Ind. Appl.*, vol. 32, no. 2, pp. 371–379, Mar./Apr. 1996.

[7] H. S. Cho, C. H. Im, and H. K. Jung, "Magnetic field analysis of 2-d permanent magnet array for planar motor," *IEEE Trans. Magn.*, vol. 37, no. 5, pp. 3762–3766, Sep. 2001.

[8] P. J. McKerrow, *Introduction to Robotics*. Sydney, Australia: Addison-Wesley, 1991.

[9] J. P. Yonnet and G. Akoun, "3D analytical calculation of the forces exerted between two cuboidal magnets," *IEEE Trans. Magn.*, vol. MAG-20, no. 5, pp. 1962–1964, Sep. 1984.

[10] J. W. Jansen, J. M. van Essen, C. M. M. van Lierop, E. A. Lomonova, and A. J. A. Vandenput, "Design and test of an ironless, three degree-of-freedom, magnetically levitated linear actuator with moving magnets," in *IEEE Int. Electric Machines and Drives Conf. (IEMDC'05)*, May 2005, pp. 858–865.

[11] J. Cao, Y. Zhu, J. Wang, W. Yin, and G. Duan, "A novel synchronous permanent magnet planar motor and its model for control applications," *IEEE Trans. Magn.*, vol. 41, no. 6, pp. 2156–2163, Jun. 2005.

[12] M.A. da Silva, A. F. F. Filho, and R. P. Homrich, "Evaluation of the normal force of a planar actuator," *IEEE Trans. Magn.*, vol. 41, no. 10, pp. 4006–4008, Oct. 2005.

[13] J. W. Jansen, C. M. M. van Lierop, E. A. Lomonova, and A. J. A. Vandenput, "Moving-magnet planar actuator with integrated active magnetic bearing," in *Proc. ASPE 2006 Annu. Meeting*, Monterey, CA, Oct. 15–20, 2006.

Manuscript received July 4, 2006; revised October 6, 2006. Corresponding author: J. W. Jansen (e-mail: j.w.jansen@tue.nl).